INTERNATIONAL JOURNAL FOR NUMERICAL METHODS IN FLUIDS
Int. J. Numer. Meth. Fluids 2007; **53**:1585–1611
Published online 27 September 2006 in Wiley InterScience (www.interscience.wiley.com). DOI: 10.1002/fld.1371

Two-dimensional MHD solver by fluctuation splitting and dual time stepping

Şölen Balcı[1,‡] and Necdet Aslan[2,*,†]

[1]*Physics Department, The Faculty of Science and Arts, Marmara University, Göztepe, 81120 Istanbul, Turkey*
[2]*Physics Department, Yeditepe University, Kayısdağı, 34755 Istanbul, Turkey*

SUMMARY

Numerical solutions of 2D magneto-hydrodynamic (MHD) equations by means of a fluctuation splitting (FS) scheme (with a new wave model and dual time stepping technique) is presented. The FS scheme, essentially based on the model explained in *Proceedings of the Tenth International Conference*, vol. 10, Swansea, 21–25 July 1997; *Godunov Symposium*, University of Michigan, Ann Arbor, 1–2 May 1997; *Physics Symposium*, Alanya, Turkey, 27–31 October 1998; *J. Comput. Phys.* 1999; **153**:437–466; *Ph.D. Thesis*, University of Marmara, Istanbul, Turkey, 2000), was extended to include gravitational source effects, limiters to limit oscillations, high order time accuracy through multistage Runge–Kutta steps, and a dual time stepping scheme to drive magnetic field divergence to zero during iterations. The numerical results show that with the new wave model called MHD-B along with its embedded numerical dissipation, correct limiting viscosity solution has been recovered and that it can safely be used in order to investigate steady or time dependent magnetized or neutral compressible flows in two dimensions. Copyright © 2006 John Wiley & Sons, Ltd.

Received 19 June 2004; Revised 16 May 2006; Accepted 6 August 2006

KEY WORDS: MHD; compressible magnetohydrodynamics; computational MHD

1. INTRODUCTION

Conservative finite difference or finite volume schemes based on higher-order Godunov methods have been effectively used to compute the solutions of hyperbolic systems of conservation laws [1–3]. Most of these schemes are based on evaluating the numerical fluxes across the neighbouring cell boundaries by means of left and right states. First FS scheme which does not require such

*Correspondence to: Necdet Aslan, Physics Department, Yeditepe University, Kayısdağı, 34755 Istanbul, Turkey.
†E-mail: naslan@yeditepe.edu.tr
‡E-mail: sbalci@marmara.edu.tr

Contract/grant sponsor: NATO

numerical fluxes has first been proposed by Roe [4, 5] in order to solve Euler Equations. The FS schemes are designed in an upwind manner since the solution residual (i.e. fluctuation) in a typical mesh is distributed only to its downstream nodes. These distributed fluctuations due to a number of waves are determined on each triangular cell by taking the area integral of flux divergence. The numerical scheme including the wave model: MHD-B differs from MHD-A mainly [6] because of a new artificial monopole function, Ψ employed to handle the divergence constraint by sub-iterations.

In the next section, the wave model MHD-B including the external source effects and the new monopole function, Ψ will be described in detail. This extended numerical method will then be used to solve two-dimensional test problems such as Kelvin–Helmholtz (KH) instability, supernovae explosions, wedge flows, etc. The numerical results of such tests presented in the last section suggest that MHD-B can be safely used in order to investigate the MHD flows and that it is more effective than MHD-A since, unlike MHD-A, the divergence constraint is handled to machine accuracy.

2. FLUCTUATION SPLITTING SCHEME WITH SOURCES

The ideal MHD equations which include the gravitational effects and new monopole function (Ψ) are given by the following conservative form with the numerical divergence source [7]:

$$\frac{\partial}{\partial t}\begin{bmatrix}\rho\\ \rho\mathbf{v}\\ \mathbf{B}\\ E\end{bmatrix}+\vec{\nabla}\cdot\begin{bmatrix}\rho\mathbf{v}\\ \rho\mathbf{v}\mathbf{v}+IP^{\star}-\dfrac{\mathbf{B}\mathbf{B}}{4\pi}\\ \mathbf{v}\mathbf{B}-\mathbf{B}\mathbf{v}+\Psi I\\ H^{\star}\rho\mathbf{v}-\dfrac{\mathbf{B}}{4\pi}(\mathbf{B}\cdot\mathbf{v}-\Psi I)\end{bmatrix}=\begin{bmatrix}0\\ -\dfrac{\mathbf{B}}{4\pi}\\ -\mathbf{v}\\ -\dfrac{\mathbf{B}\cdot\mathbf{v}}{4\pi}\end{bmatrix}\vec{\nabla}\cdot\mathbf{B}+\begin{bmatrix}0\\ -\rho\mathbf{g}\\ 0\\ -\rho\mathbf{g}\cdot\mathbf{v}\end{bmatrix} \tag{1}$$

where I is the 3×3 unit matrix, ρ is the density, $\mathbf{v}$ is the velocity, $\mathbf{B}$ is the magnetic field intensity, P is the pressure, $P^{\star}=P+B^2/8\pi$ is the total pressure, $H^{\star}=(E+P^{\star})/\rho$ is the total entalphy, $E=P/(\gamma-1)+1/2\rho v^2+B^2/8\pi$ is the total energy, γ is the ratio of specific heats, and $\mathbf{g}$ is the gravitational acceleration. Note that the divergence source appearing in Equation (1) results from inserting an artificial monopole wave into the eigen-system of MHD equations in order to stabilize them against non-zero divergence of the magnetic field. This idea was first addressed by Aslan [8], and then utilized successfully in References [9–11]. In addition, possible divergence free elements and their implementation can be found in References [12, 13]. In Cartesian geometry, the planar (v_z, $B_z=0$, $\partial/\partial z=0$) form of the MHD equations can be written as

$$\frac{\partial\mathbf{U}}{\partial t}+\vec{\nabla}\cdot\vec{\mathscr{F}}=\mathbf{S}_{\text{div}}+\mathbf{S}_{\text{grav}},\quad \vec{\mathscr{F}}=(\mathbf{F},\mathbf{G}) \tag{2}$$

where $\mathbf{U}=[\rho,\rho v_x,\rho v_y,B_x,B_y,E]^{\mathrm{T}}$ is the conservative state vector, $\mathbf{F}$ and $\mathbf{G}$ are the flux vectors given by

$$\mathbf{F}=\left[\rho v_x,\rho {v_x}^2+P^{\star}-\frac{B_x^2}{4\pi},\rho v_x v_y-\frac{B_xB_y}{4\pi},0,v_xB_y-B_xv_y+\Psi,\rho H^{\star}v_x-\frac{B_x}{4\pi}(\mathbf{B}\cdot\mathbf{v}+\Psi)\right]^{\mathrm{T}}$$

DOI: 10.1002/fld

$$\mathbf{G}=\left[\rho v_y,\ \rho v_x v_y-\frac{B_y B_x}{4\pi},\ \rho {v_y}^2+P^\star-\frac{B_y^2}{4\pi},\ v_y B_x-B_y v_x+\Psi,\ 0,\ \rho H^\star v_y-\frac{B_y}{4\pi}(\mathbf{B}\cdot\mathbf{v}+\Psi)\right]^{\mathrm{T}}$$

and $\mathbf{S}_{\mathrm{div}}$, and $\mathbf{S}_{\mathrm{grav}}$ are, respectively, divergence and gravitational sources given by

$$\mathbf{S}_{\mathrm{div}}=\vec{\nabla}\cdot\mathbf{B}\left[0,-\frac{B_x}{4\pi},-\frac{B_y}{4\pi},-v_x,-v_y,-\frac{\mathbf{B}\cdot\mathbf{v}}{4\pi}\right]^{\mathrm{T}}$$

$$\mathbf{S}_{\mathrm{grav}}=[0,\ 0,\ -\rho g,\ 0,\ 0,\ -\rho g v_y]^{\mathrm{T}}$$

where T is the transpose of the row vectors.

3. TEMPORAL DISCRETIZATION: DUAL TIME STEPPING

The MHD system given by Equation (1) has difficulties due to the divergence condition (i.e. $\vec{\nabla}\cdot\mathbf{B}=0$) which causes wrong physics if not handled properly. The time evolution of the MHD equations is performed here such that the artificial monopole function corrects the magnetic field within the pseudo iterations (τ) between the physical time levels. In these pseudo-iteration levels, Ψ is iterated until the equilibrium is reached (i.e. $\partial\Psi/\partial\tau\to 0$ thus $\vec{\nabla}\cdot\mathbf{B}\to 0$) regardless of the value of the artificial monopole parameter, α^2, defined in

$$\frac{\partial\Psi}{\partial\tau}+\vec{v}\cdot\vec{\nabla}\Psi=-\alpha^2\vec{\nabla}\cdot\mathbf{B}-\beta^2\Psi \tag{3}$$

where τ is the pseudo time step. This relaxation equation is solved for Ψ during the pseudo iterations so that by adding $\vec{\nabla}\Psi$ to the Faraday's law and its counterpart: $\mathbf{B}/4\pi\cdot\vec{\nabla}\Psi$ to the energy equation the magnetic field is corrected. Note that α^2 and β^2 in Equation (3) are relaxation constants. In addition, the terms on the right-hand side of Equation (3) can be neglected for the problems seeking steady state. This numerical technique of employing an artificial scalar function and how it is used in a relaxation scheme were explained in Reference [14]. The scheme described here is a modified version of this idea since it also includes two artificial monopole waves resulting in a more efficient divergence cleaning. In order to develop a compact scheme is done by combining the real time evolution in Equation (1) and the pseudo time relaxation equation in Equation (3). In this case, the state vector is extended to

$$\mathbf{U}=[\rho,\ \rho v_x,\ \rho v_y,\ B_x,\ B_y,\ E,\ \Psi]^{\mathrm{T}} \tag{4}$$

and Equation (3) is added to Equation (1). In this case, the following quasilinear form of MHD equations, including the effects of Ψ, is obtained:

$$\frac{\partial\mathbf{U}}{\partial\tau}+I_m\frac{\partial\mathbf{U}}{\partial t}+A_u(\alpha^2)\frac{\partial\mathbf{U}}{\partial x}+B_u(\alpha^2)\frac{\partial\mathbf{U}}{\partial y}=\mathbf{S}_u \tag{5}$$

where $I_m=\mathrm{diag}[1,\ 1,\ 1,\ 1,\ 1,\ 1,\ 0]$ is the diagonal matrix used to separate the pseudo-iterations for Ψ from the physical time iterations. Here $\mathbf{S}_u=\mathbf{S}_{\mathrm{div}}+\mathbf{S}_{\mathrm{grav}}$ are the sum of divergence and source vectors which have an additional zero component associated with Ψ. In addition, $A_u=\partial\mathbf{F}/\partial\mathbf{U}$, and $B_u=\partial\mathbf{G}/\partial\mathbf{U}$ are 7×7 the flux Jacobian matrices including the effects of Ψ in their last

DOI: 10.1002/fld

rows. Note that, this procedure is nothing but modifying the divergence condition to employ a relaxation equation for artificial magnetic monopole function in order to iterate advanced in pseudo time. In that case, the magnetic field will be corrected before the new time level is reached. When this modified equation system reaches steady state in pseudo time (i.e. $\partial\Psi/\partial\tau \to 0$) the function Ψ will have completed its role of correction and the following time accurate solution will be recovered:

$$I_m \frac{\partial \mathbf{U}}{\partial t} = \mathrm{Res}(\mathbf{U}, \alpha^2) \tag{6}$$

where

$$\mathrm{Res}(\mathbf{U}, \alpha^2) = -A_u(\alpha^2)\frac{\partial \mathbf{U}}{\partial x} - B_u(\alpha^2)\frac{\partial \mathbf{U}}{\partial y} + \mathbf{S}_u \tag{7}$$

is called the residual vector. As done in Reference [15], the real time derivative is approximated by the following second-order accurate 3-level formula:

$$\frac{\partial \mathbf{U}}{\partial t} = \frac{3}{2\Delta t}(\mathbf{U}^{n+1} - \mathbf{U}^n) - \frac{1}{2\Delta t}(\mathbf{U}^n - \mathbf{U}^{n-1}) \tag{8}$$

where n is the time step. By combining the real time levels with those of the pseudo time, one gets

$$\frac{\mathbf{U}^{n+1,m+1} - \mathbf{U}^{n+1,m}}{\Delta\tau} + I_m\left[\frac{3(\mathbf{U}^{n+1,m+1} - \mathbf{U}^n)}{2\Delta t} - \frac{(\mathbf{U}^n - \mathbf{U}^{n-1})}{2\Delta t}\right] = \mathrm{Res}^{n+1,m+1} \tag{9}$$

where m is the pseudo time iteration level. By adding and subtracting $\mathbf{U}^{n+1,m}$ to the first term in the bracket in Equation (9) and combining the resulting terms with the left-hand side, the above equation can be written as

$$\frac{\mathbf{U}^{n+1,m+1} - \mathbf{U}^{n+1,m}}{\Delta\tau} = -I'_m\left[\frac{3(\mathbf{U}^{n+1,m} - \mathbf{U}^n)}{2\Delta t} - \frac{(\mathbf{U}^n - \mathbf{U}^{n-1})}{2\Delta t}\right] + \mathrm{Res}^{n+1,m+1} \tag{10}$$

where $I'_m = [I + 1.5\Delta\tau/\Delta t\, I_m]^{-1} I_m$ is the modified diagonal matrix and I is the 7×7 unit matrix. By doing this, the time derivative term was made explicit but the residual still requires the implicit treatment. To establish that, implicit time stepping technique or explicit RK time algorithms can be employed. Although the implicit time stepping algorithms provide very quick convergence rates, it is very difficult to implement them on unstructured triangular grids. Instead, multi-stage RK algorithm given below was used to improve the solution vector for the next pseudo time iteration (with the levels m replaced by k)

$$\begin{aligned} \mathbf{U}^{n+1,k+1} &= \mathbf{U}^{n+1,k} + a^k\left[I + 1.5\frac{\Delta\tau}{\Delta t} I_m\right]^{-1} [\mathrm{Res}^{n+1,k+1}]^* \\ [\mathrm{Res}^{n+1,k+1}]^* &= \mathrm{Res}^{n+1,k} - I_m\left[\frac{3(\mathbf{U}^{n+1,k} - \mathbf{U}^n)}{2\Delta t} - \frac{(\mathbf{U}^n - \mathbf{U}^{n-1})}{2\Delta t}\right] \end{aligned} \tag{11}$$

DOI: 10.1002/fld

where k is the number of RK stages and a^k is the RK parameters. The third-order accurate RK method (used in this study) which is positive and oscillation free is given by [16]

$$\begin{aligned}\mathbf{U}^1 &= \mathbf{U}^n + \Delta t\,\mathrm{Res}(\mathbf{U}^n)\\ \mathbf{U}^2 &= \frac{3\mathbf{U}^n + \mathbf{U}^1}{4} + \frac{\Delta t}{4}\mathrm{Res}(\mathbf{U}^1)\\ \mathbf{U}^{n+1} &= \frac{\mathbf{U}^n + 2\mathbf{U}^2}{3} + \frac{2\Delta t}{3}\mathrm{Res}(\mathbf{U}^2)\end{aligned} \tag{12}$$

After the RK steps are completed, one gets $\mathbf{U}^{n+1,k+1} \to \mathbf{U}^{n+1,m+1}$ and by the end of pseudo iterations, $\mathbf{U}^{n+1,m+1} \to \mathbf{U}^{n+1}$ recovering Equation (6) and obtaining the corrected solution at the new time level $n+1$. The numerical experience shows that the pseudo iterations (including sub RK levels) usually converge within 5–10 iterations, see Figure 5. A similar form of dual time stepping algorithm was explained in Reference [15].

4. SPATIAL DISCRETIZATION AND WAVE MODEL: MHD-B

The derivation of the MHD wave model is easier when the state in primitive form (i.e. $\mathbf{W} = [\rho, v_x, v_y, B_x, B_y, P, \Psi]^{\mathrm{T}}$) is used since its eigen-system is less complicated. This primitive form can be obtained by premultiplying Equation (5) by the inverse of the matrix: $M = \partial\mathbf{U}/\partial\mathbf{W}$. This form is given by

$$\frac{\partial \mathbf{W}}{\partial t} + (A_w, B_w) \cdot \vec{\nabla}\mathbf{W} = \mathbf{S}_w \tag{13}$$

where $\mathbf{S}_w = M^{-1}\mathbf{S}_u$ and $A_w = M^{-1}A_u M$, $B_w = M^{-1}B_u M$. Model-B utilizes the matrix $A_n = (A_w, B_w) \cdot \vec{n}_\theta = A_w \cos\theta + B_w \sin\theta$ given by

$$A_n = \begin{bmatrix} v_n & \rho\cos\theta & \rho\sin\theta & 0 & 0 & 0 & 0\\ 0 & v_n & 0 & -\dfrac{B_y}{4\pi\rho}\sin\theta & \dfrac{B_y}{4\pi\rho}\cos\theta & \dfrac{\cos\theta}{\rho} & 0\\ 0 & 0 & v_n & \dfrac{B_x}{4\pi\rho}\sin\theta & -\dfrac{B_x}{4\pi\rho}\cos\theta & \dfrac{\sin\theta}{\rho} & 0\\ 0 & -B_y\sin\theta & B_x\sin\theta & v_n & 0 & 0 & \cos\theta\\ 0 & B_y\cos\theta & -B_x\cos\theta & 0 & v_n & 0 & \sin\theta\\ 0 & \gamma P\cos\theta & \gamma P\sin\theta & (\gamma-1)UB & (\gamma-1)UB & v_n & 0\\ 0 & 0 & 0 & \alpha^2\cos\theta & \alpha^2\sin\theta & 0 & 0 \end{bmatrix} \tag{14}$$

where $UB = v_x B_x + v_y B_y$ and n_θ represents the angle at which MHD waves propagate, and $v_n = \mathbf{v} \cdot \vec{n}_\theta$ is the speed along the wave propagation direction $\vec{n}_\theta$ (see References [6, 7] for details).

DOI: 10.1002/fld

Notice that the effect of Ψ is evident from the 7th row and 4–5th-columns of A_n. This 7×7 matrix has 7 eigenvalues that represent an entropy wave, two slow and two fast magneto-acoustic waves, and two new artificial magnetic monopole waves. They are given by

$$\Lambda : v_n - u_f, v_n - u_s, v_n, \lambda_m^-, \lambda_m^+, v_n + u_s, v_n + u_f \tag{15}$$

where $\lambda = v_n$ is the entropy eigenvalue, while $v_n \pm u_f$ and $v_n \pm u_s$ are fast and slow magneto-acoustic eigenvalues, respectively. Here u_f and u_s are fast and slow speeds given by

$$\begin{aligned} u_f &= [\tfrac{1}{2}[a^2 + u_B^2 + [(a^2 + u_B^2)^2 - 4a^2 u_n^2]^{1/2}]]^{1/2} \\ u_s &= [\tfrac{1}{2}[a^2 + u_B^2 - [(a^2 + u_B^2)^2 - 4a^2 u_n^2]^{1/2}]]^{1/2} \end{aligned} \tag{16}$$

with $B_n = \mathbf{B} \cdot \vec{n}_\theta$, $u_n^2 = B_n^2/4\pi\rho$, and $u_B^2 = B^2/4\pi\rho$ and $a = \sqrt{\gamma P/\rho}$, the sound speed. In addition, $\lambda^\pm$ are the artificial monopole eigenvalues given by $\lambda_m^\pm = v_n/2 \pm \sqrt{v_n^2/4 + \alpha^2}$ when the convection terms in Equation (3) are ignored. These eigenvalues turn into $\lambda_m^\pm = v_n \pm \sqrt{\alpha^2}$ when the convection terms are not neglected. In that case, the last diagonal term in the Jacobian matrix given by Equation (14) turns into v_n. The right eigenvectors of A_n are given as the following column matrix in the same order of eigenvalues given in Equation (15):

$$R_w = \begin{bmatrix} \rho & \rho & 1 & 0 & 0 & \rho & \rho \\ -r_{2f} & -r_{2s} & 0 & 0 & 0 & r_{2s} & r_{2f} \\ -r_{3f} & -r_{3s} & 0 & 0 & 0 & r_{3s} & r_{3f} \\ -r_{4f}\sin\theta & -r_{4s}\sin\theta & 0 & \cos\theta_m & \cos\theta_m & -r_{4s}\sin\theta & -r_{4f}\sin\theta \\ r_{4f}\cos\theta & r_{4s}\cos\theta & 0 & \sin\theta_m & \sin\theta_m & r_{4s}\cos\theta & r_{4f}\cos\theta \\ \gamma P & \gamma P & 0 & 0 & 0 & \gamma P & \gamma P \\ 0 & 0 & 0 & -\lambda_m^- & -\lambda_m^+ & 0 & 0 \end{bmatrix} \tag{17}$$

where $r_{2s,f}$, $r_{3s,f}$ and $r_{4s,f}$ are the same as given in References [7, 6]. Note that the last terms of the $\pm$ monopole eigenvectors turn into $\pm\sqrt{\alpha^2}$ when the convection terms in Equation (3) are retained. Since the MHD system is hyperbolic in type, the gradient in $\mathbf{W}$ can be projected onto the right eigenvectors of the matrix in Equation (14)

$$\vec{\nabla}\mathbf{W} = \sum_\kappa \alpha_\kappa \mathbf{r}_w^\kappa \vec{n}_\theta^\kappa \tag{18}$$

and the wave strength of the κth wave can be found from

$$\alpha_\kappa = l_w^\kappa \vec{\nabla}\mathbf{W} \cdot \vec{n}_\theta^\kappa \tag{19}$$

where l_w^κ is the left eigenvectors normalized by $l_w^\kappa r_w^m = \delta_{\kappa,m}$ and $\vec{n}_\theta^\kappa$ is the propagation direction of this wave. Thus, the gradient in $\mathbf{W}$ results in the following conservative state and flux vector

DOI: 10.1002/fld

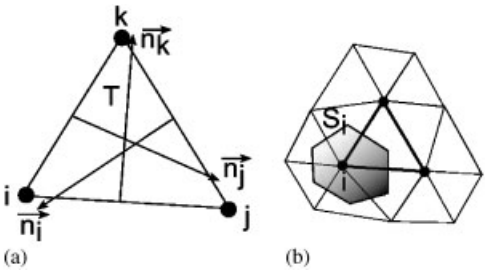

Figure 1. (a) Triangle with inward normals $\vec{n}_i = (y_j - y_k)\hat{e}_x - (x_j - x_k)\hat{e}_y$ whose lengths are equal to their associated sides; and (b) median dual cell area S_i around node i.

gradients:

$$\vec{\nabla}\mathbf{U} = \sum_{\kappa} \alpha_\kappa \mathbf{r}_u^\kappa \vec{n}_\theta^\kappa \quad \text{and} \quad \vec{\nabla}\mathbf{F} = \sum_{\kappa} \lambda_\kappa \alpha_\kappa \mathbf{r}_u^\kappa \vec{n}_\theta^\kappa \tag{20}$$

where $\mathbf{r}_u^\kappa = M\mathbf{r}_w^\kappa$ is the conservative right eigenvector.

The FS scheme presented here is developed for triangular meshes in which the physical quantities are stored on their vertices. A typical triangle and its associated median dual cell area (S_i) are shown in Figure 1. Equation (5) is solved on such a typical triangle T, by integrating it over its area, S_T

$$\Phi_T = \iint_{S_T} \mathbf{U}_t \, \mathrm{d}S = -\iint_{S_T} \left[A_u \frac{\partial \mathbf{U}}{\partial x} + B_u \frac{\partial \mathbf{U}}{\partial y} \right] \mathrm{d}S + \iint_{S_T} \mathbf{S}_u \, \mathrm{d}S \tag{21}$$

where the term Φ_T is called the fluctuation or average time rate of conservative state in the triangle. The flux integral in Equation (21) can only be evaluated approximately by means of a parameter state vector ($\mathbf{Z}$) which leads to a Jacobian which is linear in terms of its components. This parameter state vector ($\mathbf{Z}$) is assumed to vary linearly over the triangle; therefore, its cell average can be found from $\overline{\mathbf{Z}} = [\mathbf{Z}_i + \mathbf{Z}_j + \mathbf{Z}_k]/3$ where i, j, k are the vertices of the triangle (see Figure 1(a)). The form of $\mathbf{Z}$ can be found for the Euler equations uniquely by analytically solving the Rankine–Hugoniot (R–H) relations (i.e. $\vec{\nabla}\mathbf{F} = \mathbf{A}(\mathbf{Z}) \cdot \vec{\nabla}\mathbf{U}$) for the components of $\mathbf{Z}$ (here $\mathbf{F} = (F, G)$ and $\mathbf{A} = (A_u, B_u)$. In MHD constructing such a parameter vector is very complicated and impractical; therefore, an approximate form is used [6]

$$\mathbf{Z} = [\sqrt{\rho}, \sqrt{\rho}v_x, \sqrt{\rho}v_y, B_x, B_y, \sqrt{\rho}H^*, \Psi]^{\mathrm{T}} \tag{22}$$

With this parameter vector, most of the elements of Jacobians $A_z = \partial\mathbf{F}/\partial\mathbf{Z}$ and $B_z = \partial\mathbf{G}/\partial\mathbf{Z}$ will be linear in its components so that R–H conditions are approximately satisfied. Provided that such a parameter state is considered the conservative fluctuation in terms of $\overline{\mathbf{Z}}$ can be found from

$$\Phi_T = -S_T[(A_u(\overline{\mathbf{Z}}), B_u(\overline{\mathbf{Z}})) \cdot \vec{\nabla}\mathbf{U} - \mathbf{S}_u(\overline{\mathbf{Z}})] \tag{23}$$

where $\vec{\nabla}\mathbf{U} = M\vec{\nabla}\mathbf{W}$ and $\vec{\nabla}\mathbf{W} = (\overline{\mathbf{W}}_x, \overline{\mathbf{W}}_y)$ can be found from

$$\overline{W}_{x,y} = \frac{1}{S_T} \iint_{S_T} \mathbf{W}_{x,y} \, \mathrm{d}S = \left(\frac{\partial \mathbf{W}}{\partial \mathbf{Z}} \right)_{\overline{\mathbf{Z}}} \mathbf{Z}_{x,y} = M_z(\overline{\mathbf{Z}})\mathbf{Z}_{x,y} \tag{24}$$

DOI: 10.1002/fld

where $M_z = \partial \mathbf{W}/\partial \mathbf{Z}$ and $\mathbf{Z}_{x,y} = 1/S_T \sum_i \mathbf{Z}_i (\vec{n}_i)_{x,y}$. Utilizing the identities in Equations (20) in Equation (23) gives rise to the following fluctuation in T:

$$\Phi_T = -S_T \left[\sum_\kappa \lambda_\kappa^n \alpha_\kappa \mathbf{r}_u^\kappa \vec{n}_\theta^\kappa - \mathbf{S}_u(\overline{\mathbf{Z}}) \right] \tag{25}$$

where λ_κ^n is given in Equation (15).

The time rate of $\mathbf{U}_i$ in T can be written (to the first-order accuracy) as

$$\iint_{S_T} \frac{\partial \mathbf{U}}{\partial t} \, \mathrm{d}S = \frac{\mathbf{U}_i^{n+1} - \mathbf{U}_i^n}{\Delta t} S_i \tag{26}$$

where Δt is the time step and $S_i = \frac{1}{3} \sum_T S_T$ is the median dual cell area around node i (see Figure 1(b)). Taking all the triangles around node i into consideration and employing the RK time stepping technique for higher order accuracy, the time rate of $\mathbf{U}$ becomes

$$\mathbf{U}_i^{n+1,l+1} = \mathbf{U}_i^{n,l} - a^l \frac{\Delta t^n}{S_i} \sum_T \left[\sum_\kappa \beta_{i,K}^{\mathrm{T}} \Phi_T^{\kappa,l} - \frac{\mathbf{S}_u^l(\overline{\mathbf{Z}})}{3} \right] S_T \tag{27}$$

where $\Phi_T^{\kappa,l} = \lambda_\kappa^l \alpha_\kappa^l \mathbf{r}_u^{\kappa,l}$ is the conservative fluctuation associated with κth wave at lth RK iteration level, a^l are the RK parameters and $\beta_{i,\kappa}^{\mathrm{T}}$ is the distribution coefficient satisfying $\sum \beta_{i,\kappa}^{\mathrm{T}} = 1$ for consistency. Note that the source $\mathbf{S}_u(\overline{\mathbf{Z}})$ is distributed equally to the nodes of T. See Reference [17] for a review of possible distribution coefficients.

This scheme is monotone (and hence positive) under the following time step restriction for the node i of T [18]:

$$\Delta t_i = \mathrm{CFL} \frac{S_i}{|\lambda_{\max}|_i} = \mathrm{CFL} \frac{S_i}{(|\mathbf{v}| + u_f)_i} \tag{28}$$

where for local stability, the Courant (CFL) number should satisfy CFL$<$0.5. The global time step is then found by $\Delta t = \sum_i^m \max(\Delta t_i)$ where m is the total number of nodes in the mesh.

In order to increase the spatial accuracy of this scheme to second-order, the formulation presented by Sidilkover [19] can be used. Let $\Phi_i^\kappa = \beta_i{}^\kappa \Phi_T^\kappa$ and $\Phi_j^\kappa = \beta_j{}^\kappa \Phi_T^\kappa$ be the partial residuals assigned for updating the vertices i and j, respectively, for the two node update case. Then the second-order scheme is obtained by the following corrected residuals:

$$\Phi_i^* = \Phi_i^\kappa - L\left(-\frac{\Phi_i^\kappa}{\Phi_j^\kappa}\right), \quad \Phi_j^* = \Phi_j^\kappa - L\left(-\frac{\Phi_j^\kappa}{\Phi_i^\kappa}\right) \tag{29}$$

where $L(x/y)$ is the limiter function, employed in conventional upwind schemes [18], which should satisfy (for positivity)

$$\Psi(1) = 1, \quad \Psi \geqslant 0, \quad \frac{\Psi(r)}{r} \leqslant 1$$

In this work, the following limiters which satisfy the local and global positivity are utilized [19]: Minmod: $\Psi(r) = \frac{1}{2}(1 + \mathrm{sgn}(r)) \min(r, 1))$, Superbee: $\Psi(r) = \frac{1}{2}(1 + \mathrm{sgn}(r)) \max(\min(2r, 1), \min(r, 2))$ where $\mathrm{sgn}(r)$ is the sign of r.

DOI: 10.1002/fld

5. WAVE MODEL FOR MHD EQUATIONS

Equation (18) shows that the gradients (i.e. the x and y derivatives) of $\mathbf{W}$ is constructed by the sum of wave fluctuations. Provided that W_x and W_y are found from Equation (24), they can be written from Equation (18) as

$$\begin{aligned}\mathbf{W}_x &= \alpha_e^1 \mathbf{r}_e^1 \cos\theta_e + \sum_{\kappa=2}^{3} \alpha_m^\kappa \mathbf{r}_m^\kappa \cos\theta + \sum_{\kappa=4}^{7} \alpha_\theta^\kappa \mathbf{r}_\theta^\kappa \cos\theta - \sum_{\kappa=8}^{11} \alpha_{\theta+\pi/2}^\kappa \mathbf{r}_{\theta+\pi/2}^\kappa \sin\theta \\ \mathbf{W}_y &= \alpha_e^1 \mathbf{r}_e^1 \sin\theta_e + \sum_{\kappa=2}^{3} \alpha_m^\kappa \mathbf{r}_m^\kappa \sin\theta + \sum_{\kappa=4}^{7} \alpha_\theta^\kappa \mathbf{r}_\theta^\kappa \sin\theta - \sum_{\kappa=8}^{11} \alpha_{\theta+\pi/2}^\kappa \mathbf{r}_{\theta+\pi/2}^\kappa \cos\theta\end{aligned} \tag{30}$$

Among the total of 11 waves, the first one denotes the entropy wave, the first sum corresponds to backward and forward artificial monopole waves, the second sum represent the backward and forward slow and fast magneto-acoustic waves, and finally the last sum coincide with the magneto-acoustic waves propagating perpendicularly to former magneto-acoustic waves.

When Equations (30) are written explicitly, one can solve the propagation angle and the strength of entropy wave given by (the same as in MHD-A [4, 11])

$$\tan\theta_e = \frac{(\rho_y - (P_y/a^2))}{(\rho_x - (P_x/a^2))}, \quad \alpha_e = \sqrt{\left(\rho_x - \frac{P_x}{a^2}\right)^2 + \left(\rho_y - \frac{P_y}{a^2}\right)^2} \tag{31}$$

When convection terms in Equation (3) are neglected, the artificial backward and forward magnetic monopole wave strengths and their propagation directions are given by (different from single monopole wave in MHD-A [4, 6])

$$\alpha_m^2 = \alpha_m^- = -\frac{\sqrt{(\Psi_x^2 + \Psi_y^2)} + \lambda_m^+ \vec{\nabla}\cdot\mathbf{B}}{2u_m}, \quad \alpha_m^3 = \alpha_m^+ = \frac{\sqrt{(\Psi_x^2 + \Psi_y^2)} + \lambda_m^- \vec{\nabla}\cdot\mathbf{B}}{2u_m} \tag{32}$$

$$\theta_m = \tan^{-1}\frac{\Psi_y}{\Psi_x} \tag{33}$$

where $u_m = \sqrt{v_n^2/4 + \alpha^2}$ and α_m^- and α_m^+ satisfying $\alpha_m^- + \alpha_m^+ = \vec{\nabla}\cdot\mathbf{B}$ and corresponding to the single monopole wave of MHD-A. In addition, these wave strengths assume the forms: $\alpha_m^2 = \frac{1}{2}[\vec{\nabla}\cdot\vec{B} - \sqrt{\Psi_x^2 + \Psi_y^2}]$, $\alpha_m^3 = \frac{1}{2}[\vec{\nabla}\cdot\vec{B} + \sqrt{\Psi_x^2 + \Psi_y^2}]$ when the convection terms in Equation (3) are not ignored.

Since Ψ is assumed to vary linearly over the triangle (see Equation (22)), Ψ_x and Ψ_y can be found from $\Psi_{x,y} = 1/S_T \sum_i \Psi_i (\vec{n}_i)_{x,y}$. Obviously, this wave has no action when the divergence condition is exactly satisfied (i.e. $\vec{\nabla}\cdot\mathbf{B} = 0$). The dissipation effect of this wave becomes significant relevant only in the regions where the divergence condition is violated because of discretization errors. One can also show that the propagation direction of magneto-acoustic waves is given by

DOI: 10.1002/fld

(the same as in Reference [11])

$$\tan 2\theta = \frac{(B_x)_y + (B_y)_x}{(B_x)_x - (B_y)_y} \tag{34}$$

The strengths of the slow and fast magneto-acoustic waves are given by

$$\alpha_\theta{}^{4/5} = \mp l_{3f}{}^\theta[\vec{\nabla} v_x \cdot \vec{n}_\theta] \mp l_{2f}{}^\theta[\vec{\nabla} v_y \cdot \vec{n}_\theta] - l_{4f}{}^\theta \vec{\nabla} P \cdot \vec{n}_\theta + \frac{B_\perp[(B_x)_y - (B_y)_x]}{16\pi\rho(u_f^2 - u_s^2)} \tag{35}$$

$$\alpha_\theta{}^{6/7} = \pm l_{3s}{}^\theta[\vec{\nabla} v_x \cdot \vec{n}_\theta] \pm l_{2s}{}^\theta[\vec{\nabla} v_y \cdot \vec{n}_\theta] + l_{4s}{}^\theta \vec{\nabla} P \cdot \vec{n}_\theta - \frac{B_\perp[(B_x)_y - (B_y)_x]}{16\pi\rho(u_f^2 - u_s^2)} \tag{36}$$

where $\vec{\nabla} P \cdot \vec{n}_\theta = P_x \cos\theta + P_y \sin\theta$ is the pressure gradient projected onto the wave propagation direction and $l_{2s,f}$, $l_{3s,f}$ and $l_{4s,f}$ were given in References [6, 7, 20–22]. Note that the denominators of Equations (35) and (36) cannot vanish unless the pressure and hence the sound speed vanishes. Replacing the angle θ with $\theta + \pi/2$ in Equations (35) and (36) leads to the remaining wave strengths $\alpha_{\theta+\pi/2}^{8/9}$ and $\alpha_{\theta+90}^{10/11}$.

The main differences between models MHD-A and B are that model-B includes another variable, Ψ and it includes two divergence waves moving in opposite directions while model-A includes single divergence wave with wave strength directly related to $\vec{\nabla} \cdot \vec{B}$. The effects of Ψ is seen in the last rows and columns of the Jacobian matrix given in Equation (14). Since, the strengths of these new monopole waves differ in these directions, they can operate in a wider region to detect points at which $\vec{\nabla} \cdot \vec{B}$ tends to increase. In addition, extra dissipation has the effect of reducing local errors due to $\vec{\nabla} \cdot \vec{B} \neq 0$. The numerous tests and the results presented in this paper shows that MHD-B leads to slightly less divergence errors than model-A. This shows that, different numerical models can be developed in the future to further reduce divergence errors.

5.1. Solution algorithm

The solution algorithm of the code developed here can be explained as follows: For each triangle, T

1. get $\rho, v_x, v_y, B_x, B_y, E$ from the solutions of the elements of conservative state vector and determine pressure from the equation of state: $P = E/(\gamma - 1) - 1/2\rho v^2 - B^2/8\pi$. By using the nodal values of the primitive state obtain $\mathbf{Z}$ from Equation (22), i.e. the parameter state, for each node i of T, and then using the matrix: $\partial\mathbf{W}/\partial\mathbf{Z}$ determine mesh averaged primitive state: $\overline{\mathbf{W}} = [\overline{\rho}, \overline{v_x}, \overline{v_y}, \overline{B_x}, \overline{B_y}, \overline{P}, \overline{\Psi}]^{\mathrm{T}}$,
2. using 3 nodal values of T, find the mesh averaged parameter vector, and its gradient from $\overline{\mathbf{Z}} = \frac{1}{3}\sum_{m=1}^{3} \mathbf{Z}_m$ and $\vec{\nabla}\mathbf{Z} = 1/2S_T \sum_{m=1}^{3} \vec{n}_m \mathbf{Z}_m$,
3. obtain the x and y derivatives of $\mathbf{W}$ from Equation (24),
4. find the propagation angles θ_e, θ_m and θ from Equations (31)–(34),
5. using these angles and averages, find $v_n = v_x \cos\theta + v_y \sin\theta$ and evaluate $\overline{Z}, \overline{u}_f, \overline{u}_s$ from Equations (16) and get the averaged sound speed from $\overline{a} = \sqrt{\gamma \overline{P}/\overline{\rho}}$,

DOI: 10.1002/fld

6. get all wave strengths from Equations (31), (32), (35), (36), the eigenvalues from Equation (15), the right primitive eigenvectors, $\overline{r}_w$ from Equation (17), and the conservative eigenvectors, $\overline{r}_u$ using the matrix: $\partial\mathbf{U}/\partial\mathbf{W}$,
7. having determined the eigen-system of 7 individual waves for each wave, k
   7.1. get the wave fluctuation from Equation (25) using the averaged values: $\overline{\lambda}_k$, $\overline{\alpha}_k$ and $\overline{r}_u^k$,
   7.2. using the mesh properties and $\vec{n}(\theta) = (\cos\theta, \sin\theta)$, determine the upwind nodes for this wave and assign $\overline{\Phi}_k$ to these nodes of T using the distribution technique described in References [19] or [23].

After the contributions of each wave k are obtained at the nodes of the triangles and all the triangles around nodes are visited, the nodal mesh updates will have been completed and the nodal values will have reached their values at the new time step, $n+1$, see Equation (27).

In this work, the time update given by Equation (27) was carried out by third-order Runge–Kutta (RK) method for improved time accuracy of the scheme. This third-order accurate RK method which is positive and oscillation free is given by Equation (12).

The viscous effects (in the form of $\nu\nabla^2\mathbf{U}$) can be simply included in the scheme by adding $\nu/4S_T\sum_{m=1}^{3}\mathbf{n}_i\cdot\mathbf{n}_m\mathbf{U}_m$ to the residual at node: i of triangle T, see p. 45 of Reference [23].

It must be noted that this scheme can also be extended into three dimensions by considering a three-dimensional mesh including tetrahedra with four faces and 4 nodes on their corners. In this case, the area integrals in Equations (21)–(26) turn into volume integrals and the inward normals shown in Figure 1(a) turn into inward normals which are perpendicular to the faces of tetrahedra with lengths equal to the face area. In addition, the gradients can be simply obtained by using, for example: $\vec{\nabla}\mathbf{Z} = \frac{1}{2V_T}\sum_{m=1}^{4}\vec{n}_m\mathbf{Z}_m$ where V_T is the volume and $m = 1-4$ are the nodes of tetrahedra, see Reference [23]. The 3D version of this code is currently being developed by the second author of this paper.

6. NUMERICAL RESULTS

In order to present the capability of the new scheme described here, a number of test problems were solved on a variety of meshes. The resulting graphs of the physical quantities such as density, pressure, Mach number and magnetic pressure are presented along with accuracy study, residual and divergence convergence errors. Some of the test problems were solved with both the older scheme: MHD-A and the new scheme: MHD-B. Comparisons show that the new scheme is as good as the previous one (mostly better) and that it can safely be used to investigate the magnetized flows including shocks.

6.1. Supersonic shock reflection

The first test problem is the MHD version of classical Mach = 2.9 flow in a rectangular domain of $x \in [0, 4]$ and $y \in [0, 1]$, see Reference [11] for the details. This is an excellent shock reflection test to show how the new monopole waves are able to eliminate divergence errors so that physically correct solutions (i.e. a 29° supersonic shock with $\gamma = 1.4$) reflecting from the lower boundary are obtained.

DOI: 10.1002/fld

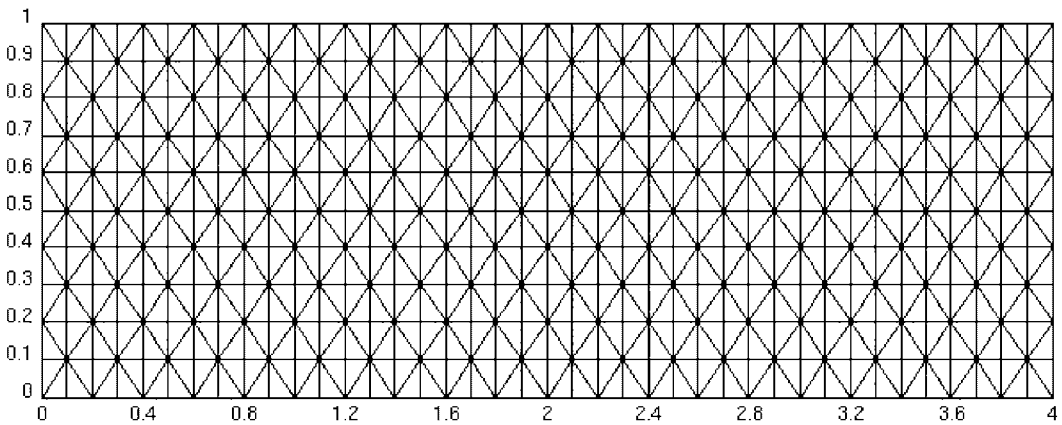

Figure 2. A typical isotropic mesh used for the shock reflection test.

The analytical boundary conditions on the left and upper boundaries are (see Reference [6])

$$\mathbf{W}^L = [1, 2.9, 0, \sqrt{\pi}, 0, 1/\gamma]^{\mathrm{T}}, \quad \mathbf{W}^U = [1.46, 2.717, -0.405, 2.424, -0.361, 1.223]^{\mathrm{T}}$$

while the lower and right boundaries were chosen to be reflective and outgoing, respectively. The only action performed was to set v_y to zero on the lower boundary to accomplish reflection and the states on the right boundary were simply untouched during iterations so that this boundary is treated as outgoing.

By using the left state values as initial conditions, this test problem was solved (by both model-A and new model MHD-B) on 41×11, 81×21, and 161×41 isotropic meshes (see such a mesh in Figure 2) until $t = 10$ (with nearly 4000 iterations with a CFL number of 0.4). The resulting divergence errors and maximum residuals for these meshes are presented in Figure 3 as a function of time. As seen, the divergence error reduces as the mesh is made finer, a requirement for the scheme convergence. In addition, the results obtained by model: MHD-B produces less divergence errors although the residual errors are comparable with those of model-A. These results show that model MHD-B provides slightly better accuracy than MHD-A for such a steady state problem. Note that, in order to compare both models, the dual time stepping technique described in Section 3 was not activated in the computer code to obtain an identical comparison among the graphs of Figure 3. In both models, third-order RK time stepping was used with a CFL number of 0.4.

By using the readily available data in the residual and divergence convergence graphs in Figure 3, one can plot the convergence characteristics as a function of number of grids. According to these data values, one can see that the errors reduce as the number of grid points is increased (i.e. as the mesh is made finer). This result is presented in Figure 4. During the pseudo iterations the residual drops to a prescribed tolerance with a number of iterations. This situation is presented in Figure 5 for the current test problem. As seen, the convergences are exponential and the necessary number of iterations reduce in time. This shows the good convergence characteristics of model-B presented here. Figure 6 shows the density and Mach number contours on two different isotropic meshes for models MHD-B and MHD-A (at $t = 4$), respectively. As seen, the reflected shock is as sharp as the incident one and there exists no problems on the outgoing boundary. The graphs

DOI: 10.1002/fld

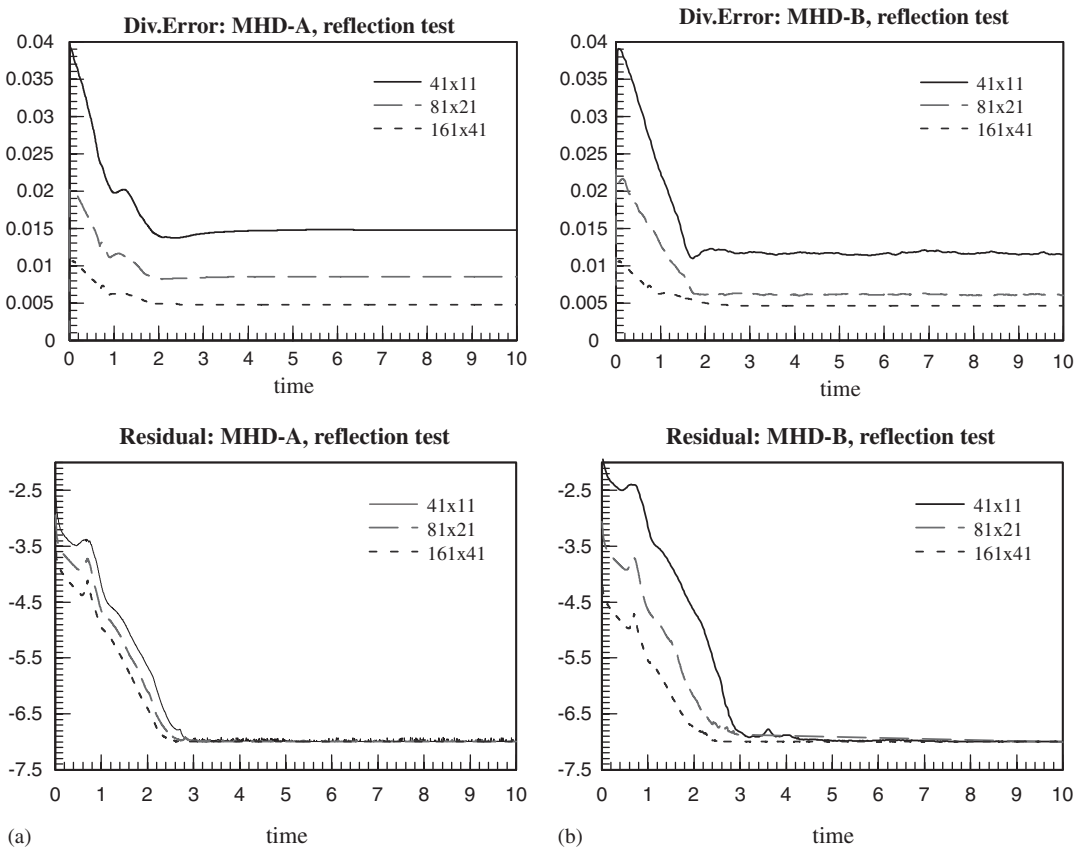

Figure 3. The divergence error and residual for model: (a) MHD-A; and (b) MHD-B as a function of time for shock reflection test on 41×11, 81×21 and 161×41 isotropic meshes.

in this figure show that MHD-A and MHD-B produce similar results although, MHD-B leads to less divergence errors.

6.2. *Kelvin–Helmholtz instability*

The second test problem is the Kelvin–Helmholtz (KH) instability, a vortex flow which arises from the velocity shear between two fluid media flowing in opposite directions. When this instability takes place, rotating vortices appear near the initial boundary between the fluids. It must be noted that the gravitational effects are ignored in this test. For the simplest case, a rapidly changing velocity profile in y direction from v_1 to v_2 (the velocities on the two sides of the interface) is used. In this case, the instability takes place if the velocity jump satisfies [24]

$$\Delta v = |v_1 - v_2| > 2u_B \tag{37}$$

where $u_B = \sqrt{B_x^2/4\pi\rho}$ is the Alfven velocity and B_x is the x-component of the magnetic field that can stabilize this instability (see Figure 7). Whether initial velocity jump causes K–H

DOI: 10.1002/fld

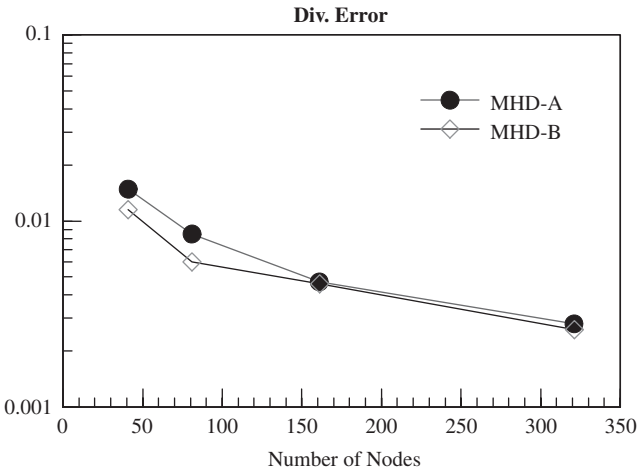

Figure 4. The mesh convergence as a function of number of grid points.

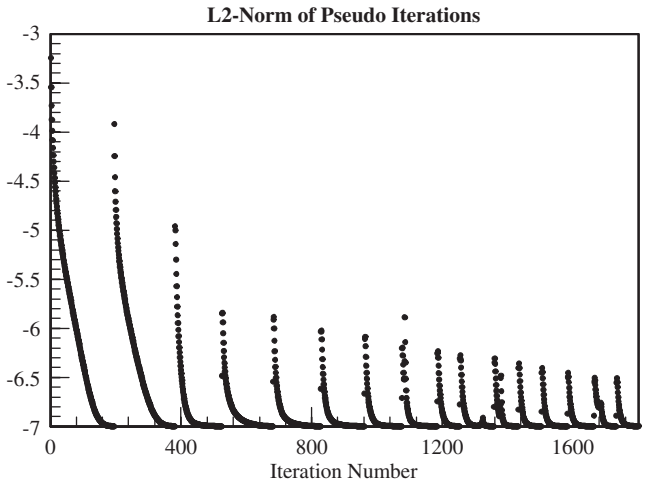

Figure 5. The pseudo convergence as a function of time iterations for shock reflection test.

instability or not depends on the horizontal magnetic field strength. Assume that the velocity jump in y direction is 5 and that $\rho = 1$ and $B_{x0} = \sqrt{4\pi}$ are considered. In this case one gets $u_B = 1$ which is smaller than $\Delta v = 5$, thus the K–H instability is expected to take place giving rise to rotating vortices and fluid mixture. When the field strength is tripled, i.e. $B_{x0} = 3\sqrt{4\pi}$ taken one gets $u_B = 3$ and since $\Delta v < 2u_B$, the K–H instability is expected to be stabilized during the time evolution. This problem was solved on 91×181 isotropic triangular grid of $x \in [0, 1]$, $y \in [-1, 1]$ with the dual time stepping algorithm employed. The boundary conditions on the left and right boundaries were taken as periodic and the other boundaries were assumed to be outgoing (free) boundaries

DOI: 10.1002/fld

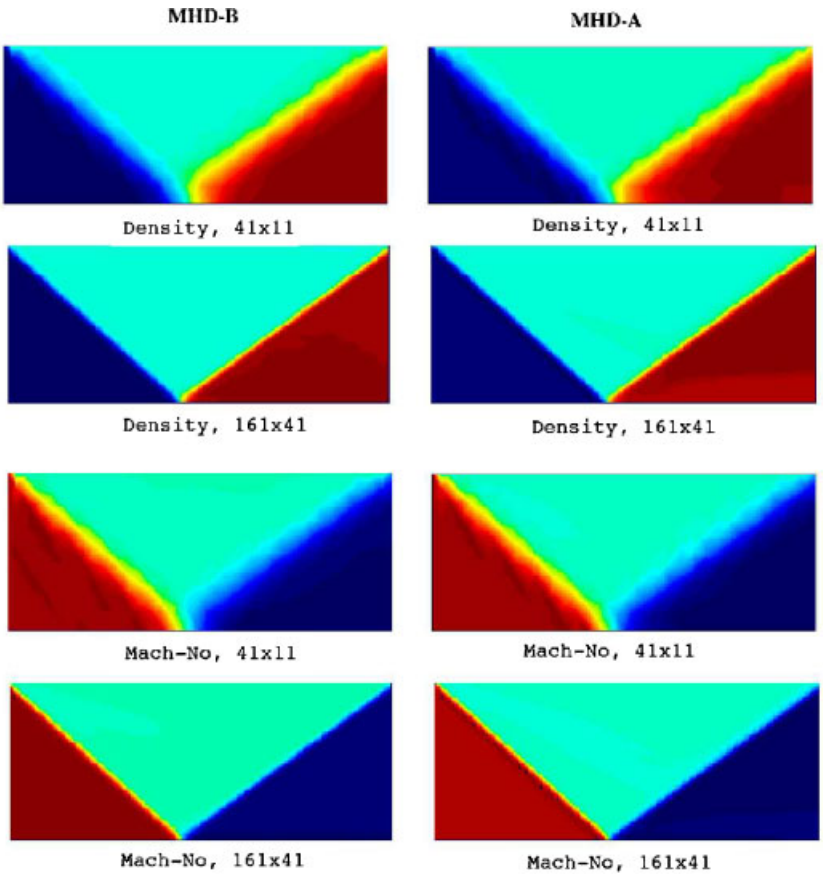

Figure 6. The density, and Mach number contours for shock reflection test on 41×11 and 161×41 isotropic meshes for models MHD-B and MHD-A.

(see Figure 7). The initial conditions with a jump in v_x and a small perturbation in v_y are given as follows:

$$v_x = 5\tanh(20y), \quad v_y = 0.25\sin(2\pi x)\mathrm{e}^{-100y^2}$$

$$\mathbf{g} = 0, \quad \rho = 1, \quad B_x = B_{x0}, \quad B_y = 0, \quad P = 50, \quad \gamma = 1.4$$

With this initial configuration, a shear region is introduced along the interface at $y = 0$ separating the fluids moving above and below it. Note that the instability is activated by the y component of the velocity given as a small perturbation. Figure 8 shows the resulting density graphs at two different times for the weak magnetic field. As seen, initially constant density and velocity jump creates rotating vortices and K–H instability develops leading to the mixing of fluids on both sides of the shear layer.

DOI: 10.1002/fld

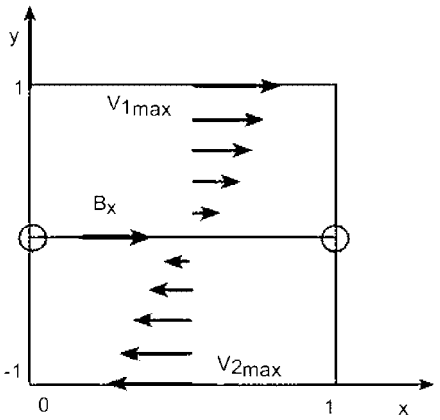

Figure 7. The initial velocity profile for the Kelvin test.

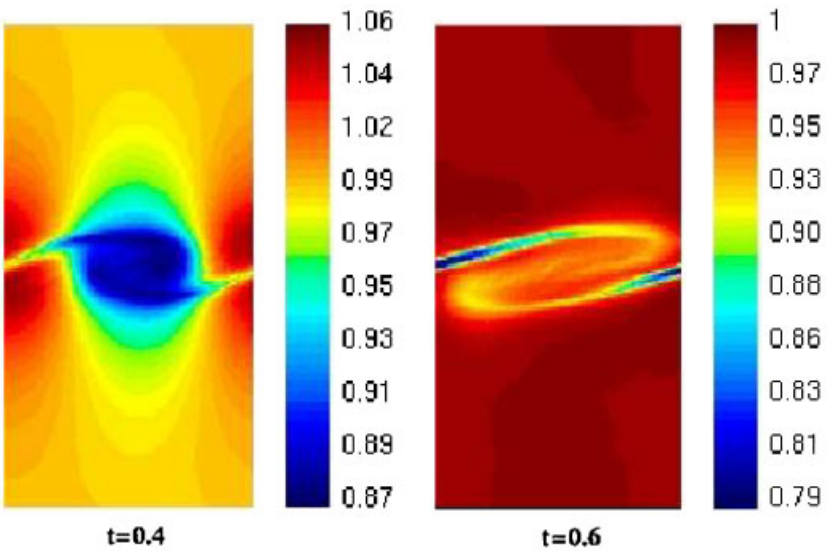

Figure 8. Density graphs for Kelvin–Helmholtz test with weak field on 91×181 iso mesh at different times.

The same test problem was also solved for a strong magnetic field ($B_{x0} = 3\sqrt{4\pi}$) using the same procedure. The resulting density graphs are shown in Figure 9. As seen, when the magnetic field along the shear layer is so strong that the opposite flows along the boundary do not mix with each other and that the rotating vortices do not appear in the shear layer during the time evolution. These results show that the numerical results are consistent with physical expectations for the Kelvin–Helmholtz instability. These results are similar to those obtained by Frank *et al*. [24] where physical resistivity and viscosity are used.

DOI: 10.1002/fld

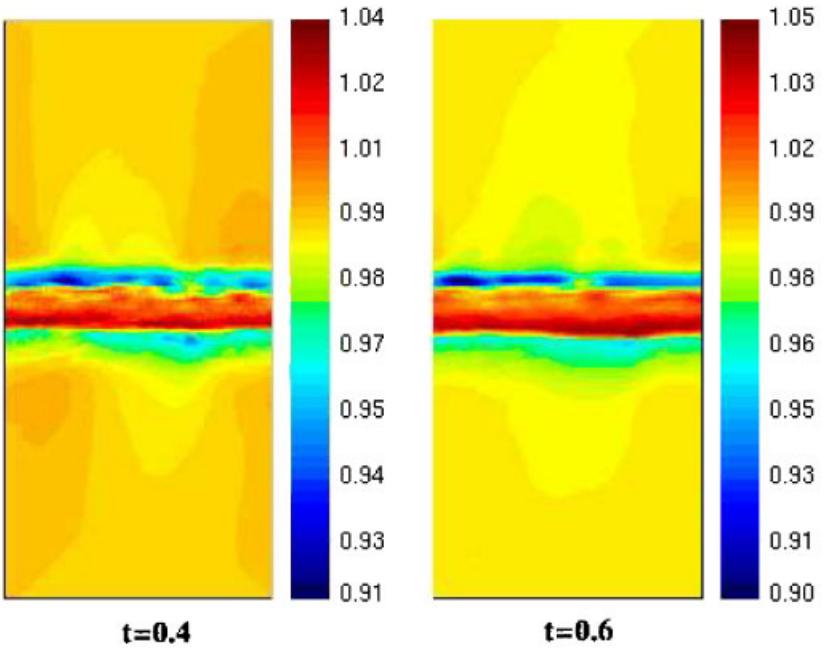

Figure 9. Density graphs for Kelvin Helmholtz test (with strong magnetic field) on 91×181 iso mesh at different times.

6.3. *Wedge flow test problem*

This test problem is a stationary wedge flow over $\theta = 30°$ wedge. This test was solved on a mesh of $x \in [0, 1]$, $y \in [y(x), 1]$ where $y(x)$ defines the wedge. A uniform supersonic horizontal inflow with a horizontal magnetic field of $B_x = 4\sqrt{4\pi}$ is imposed on the left boundary, with

$$v_x = 8, \quad v_y = 0, \quad \rho = 1, \quad P = 1, \quad \gamma = 5/3$$

The sonic and Alfvenic inflow Mach numbers are thus $M = 8\frac{\sqrt{3}}{\sqrt{5}}$ and $M_A = \sqrt{v_x^2 + v_y^2}/u_B = 2$ so the flow is supersonic and super-Alfvenic. At the lower and upper boundaries ideal wall symmetry conditions are imposed. The wedge geometry causes the formation of a fast MHD shock through which the plasma flows out freely at $x = 1$. The lower boundary is described by $y(x) = 0$ for $x \in [0, 0.3]$ and $y(x) = \tan(30°)(x - 0.3)$ for $x \in [0.3 + 0.1\cos(30°), 1]$. Figure 10 shows the density graphs obtained at $t = 0.8$ (at which the steady-state is achieved) on three different left diagonal meshes. Note that no special action is performed on the tip of the wedge in order to make the strong plane discontinuity stable. In Figure 11, the density profiles in x direction at $y = 0.7$ are shown as a function of grid resolution. As seen from these figures, the solutions at increasing resolution display convergence. These results agree well with those presented in Reference [25].

DOI: 10.1002/fld

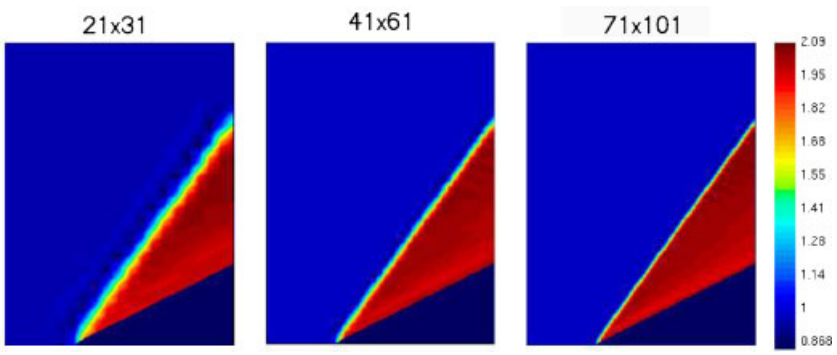

Figure 10. Density graphs obtained at $t = 0.8$ (steady-state) on the 21×31, 41×61, 71×101 left diagonal meshes.

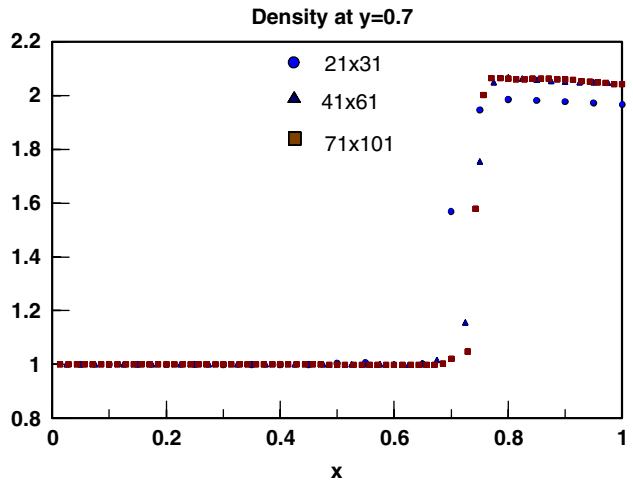

Figure 11. Density profiles for the wedge problem at $y = 0.7$ for different left diagonal meshes.

6.4. *Supersonic channel flow*

In this test problem, a steady state supersonic flow through a channel which has a smoothly varying cross section (i.e. the bottom wall with a sine square profile) is solved. The domain considered is a rectangular channel with $x \in [0, 7]$, $y \in [0, 1]$ and the bottom profile is given by $y(x) = 0.2 \sin^2[\pi(2 - x)/4]$ for $x < 2$ else $y = 0$. A typical isotropic mesh used in calculations is shown in Figure 12. A uniform supersonic horizontal inflow with horizontal magnetic field is imposed at the left boundary, $x = 0$, with

$$v_x = 2\sqrt{\gamma}, \quad v_y = 0, \quad B_x = \sqrt{4\pi}, \quad B_y = 0, \quad \rho = 1, \quad P = 1, \quad \gamma = 5/3$$

The sonic and Alfvenic inflow Mach numbers are thus $M = 2$ and $M_A = \sqrt{v_x^2 + v_y^2}/u_B = 2\sqrt{\gamma}$. At $y = 0$ and $y = y(x)$, ideal wall symmetry conditions are imposed and the plasma is allowed to

DOI: 10.1002/fld

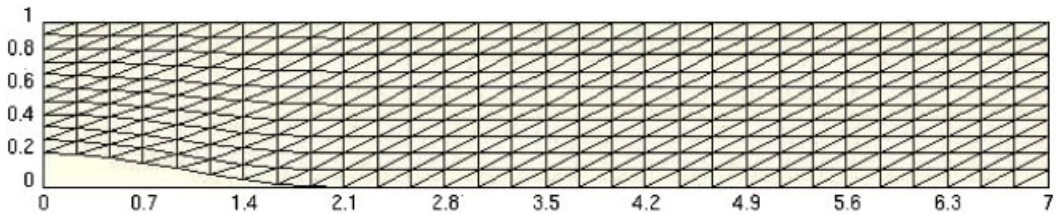

Figure 12. A typical mesh with right running diagonal triangles.

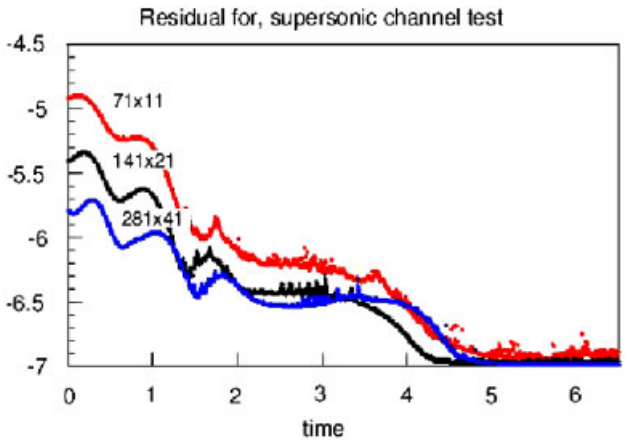

Figure 13. Residuals for supersonic channel flow for different mesh resolutions obtained for Euler limit, i.e. $B = 0$.

flow out freely at $x = 7$, where the (horizontal) out flow is supersonic. Figure 13 shows the time behaviour of the log of maximum solution residual on three different meshes in order to present the convergence property of the scheme for the Euler limit (i.e. $\mathbf{B} = 0$). As seen, the residual gets smaller and it remains constant after nearly $t = 5$ for all the meshes. Figure 14 shows the density and Mach number graphs at 281×41 mesh obtained at $t = 6$ and Figure 15 shows the x-profiles Mach number obtained at $y = 0.3$ and at $y = 0.7$ at the same time on the 281×41 mesh. The Mach number profile in Figure 5.19 of Reference [23] for $y = 0.3$ maximizes to 2.42, 2.51, 2.32 at $x = 1.8$, 5.1, and 6.5, respectively, for a very fine grid of 114 990 nodes. It can be seen that our results with only 11 521 nodes agree well with these results as Figure 15 is examined. The results at $y = 0.7$ also agree well with those in Reference [23]. The same problem was solved on the same mesh with the existence of a horizontal initial magnetic field of $B_x = 1$. The resulting log of solution residual as a function of time and the density and pressure graphs are shown in Figures 16 and 17, respectively. As seen from these figures, the convergence is good and the horizontal field alters the compression fan above the tip of the bottom profile causing more reflections from the upper wall. These results show how a horizontal magnetic field alters the flow structure inside the supersonic channel when the fluid is charged.

DOI: 10.1002/fld

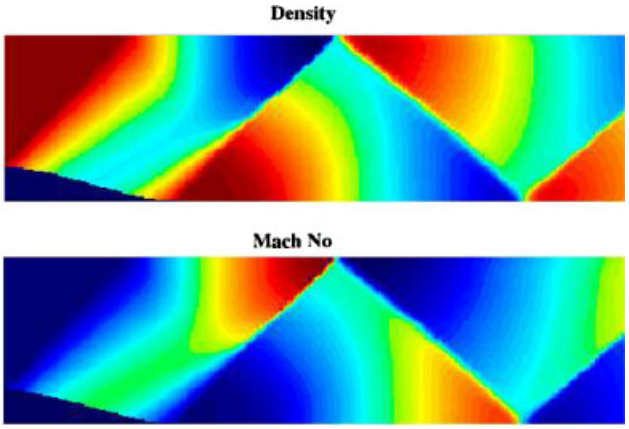

Figure 14. Density and Mach number graphs obtained at 281×41 mesh at $t = 6$ (for Euler limit, i.e. $B = 0$).

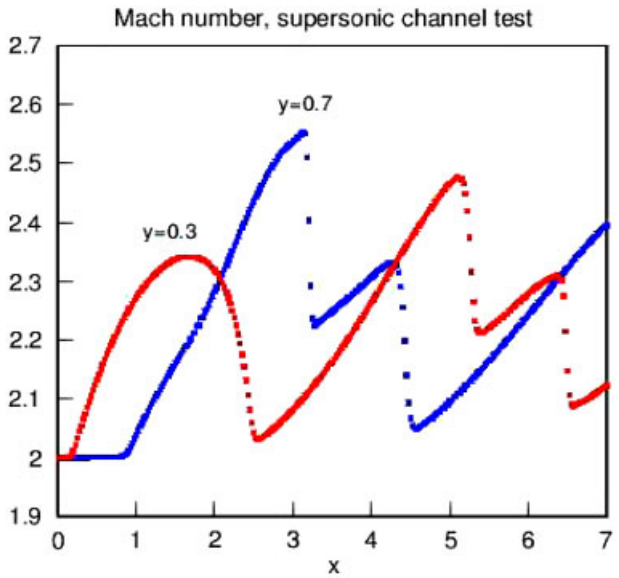

Figure 15. Mach number profiles in x direction (for Euler limit, i.e. $B = 0$).

6.5. *Explosion tests*

In this test, the free expansion of a high pressured gas (confined in a circular region) into the free medium is presented. This problem was solved with no magnetic field (i.e. $\mathbf{B} = 0$, Euler limit) and with a strong magnetic field of $B_y = 100$ as done in Reference [26]. The solution

DOI: 10.1002/fld

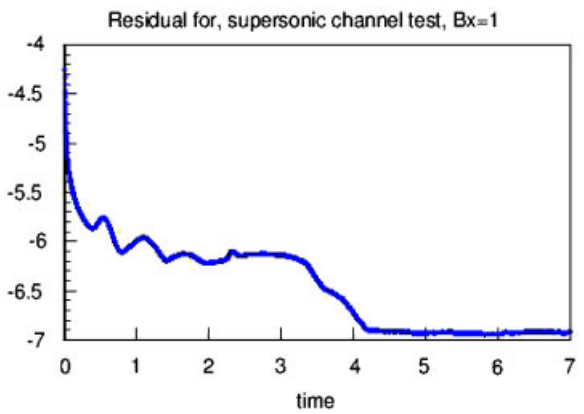

Figure 16. The residual time history for supersonic channel test for $B_x = 1$ case.

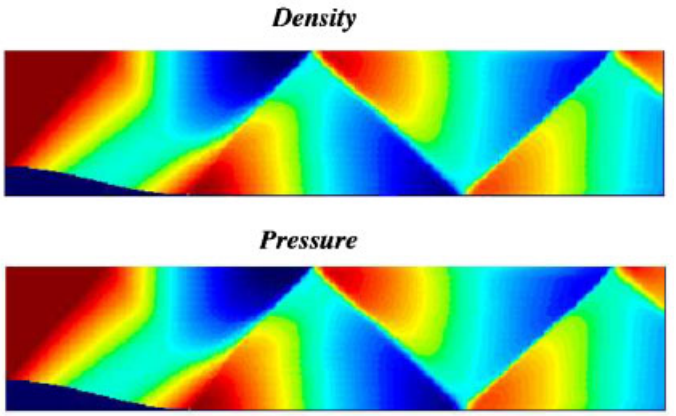

Figure 17. Density and pressure graphs at $t = 6$ on 281×41 mesh for $B_x = 1$ case.

domain considered was $x \in [-50, 50]$ and $y \in [-50, 50]$ and the high pressure region is centred within a radius of $r = 10$. Initially $\rho = 1$, $\vec{v} = 0$ and $\gamma = 2$ were taken and $P_{\text{in}} = 100$ and $P_{\text{out}} = 1$ were considered. The problem with no magnetic field was solved on 241×241 isotropic mesh with a CFL number of 0.8 until the steady-state conservation is established. The resulting density, pressure, kinetic energy, and Mach number contours at $t = 3$ are shown in Figure 18. In addition, Figure 19(a) shows the density profiles obtained at $y = 0$ on the 61×61, 121×121, 241×241 meshes. Figure 19 also includes the scanned density profile obtained in Reference [26]. As seen, Figures 19(a) and 19(b) (scanned from Reference [26]) are almost identical; thus it can be said that the results presented here agree very well with those of Reference [26]. This shows that the code performs very well whenever planar or circular symmetry exists in the solutions when magnetic field vanishes. The solutions show anisotropy when strong magnetic field

DOI: 10.1002/fld

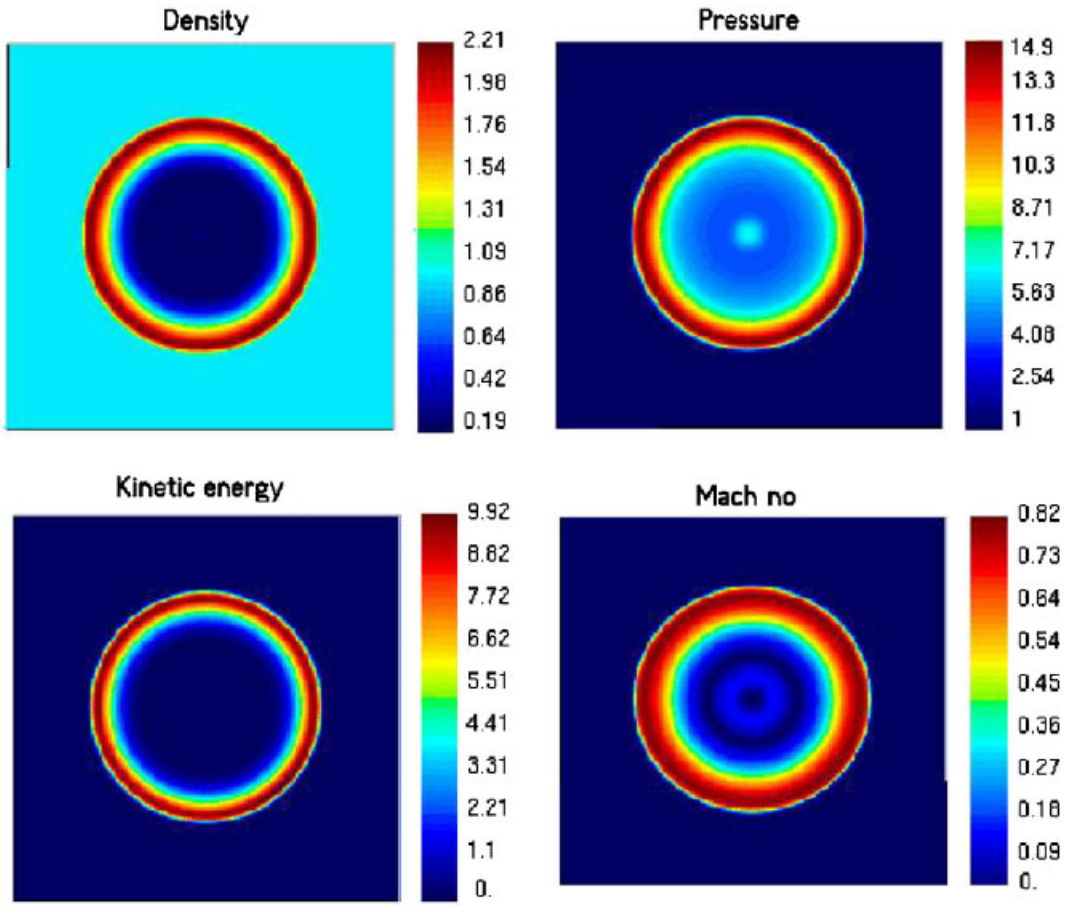

Figure 18. The solution of explosion case with $B_y = 0$ on 241×241 isotropic mesh at $t = 3$.

is applied as shown in Figure 20 where a strong magnetic field (i.e. $B_y = 100$) case were presented. These results are also similar to those presented in Reference [26].

6.6. *Gravitation test: superbubble explosion*

This problem is an astrophysical superbubble explosion test that includes the gravitational effects. The initial conditions (same as those given by Mineshige *et al*. [27]) are such that the density, pressure and horizontal magnetic field changes in the vertical direction. An intense explosion is initiated within a spherical region of a small radius by a high pressure such that the temperature and plasma beta remains constant everywhere initially.

The medium is an ideal gas, with the ratio of specific heats of $\gamma = 5/3$, the fields are chosen as: $\mathbf{v} = 0$, $B_y = 0$, $B_x \neq 0$, and the gravity in the y direction ($\mathbf{g} = -g_0 \hat{e}_y$) is constant. According to

DOI: 10.1002/fld

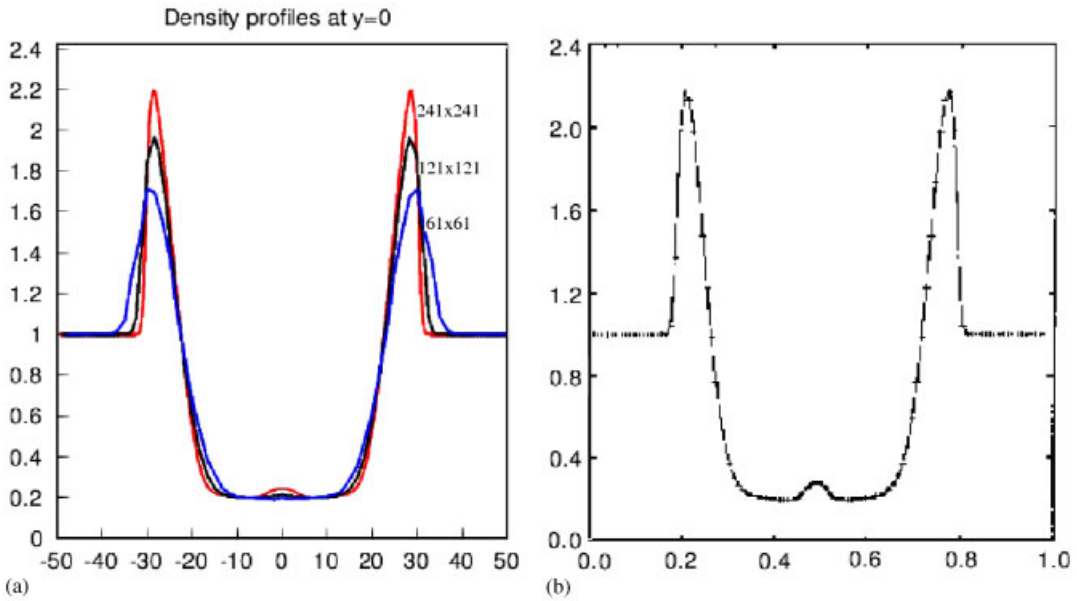

Figure 19. Density profiles for the explosion test for the Euler limit along $y=0$, the centreline: (a) the current solutions; and (b) the solution obtained by Reference [26] with 100×100 finite difference grid points.

these assumptions, the steady-state ($\partial/\partial t \to 0$) momentum equation in y direction becomes

$$\frac{\partial}{\partial y}\left(P + \frac{B_x^2}{8\pi}\right) = -\rho g \tag{38}$$

Note that, the divergence condition requires $\partial B_x/\partial x = 0$ and this results in $\partial P/\partial x = 0$ showing that the magnetic field and pressure is independent of x. Using the definition of initial constant plasma beta ($\beta = P/B_x^2/8\pi$) and the ideal equation of state (EOS) given by

$$P = \rho RT/\mu \tag{39}$$

where μ is the molecular weight, in this equation one gets

$$RT/\mu\left(1 + \frac{1}{\beta}\right)\frac{\partial \rho}{\partial y} = -\rho g \tag{40}$$

whose solution leads to the following an exponential profile in density, pressure, and horizontal magnetic field as follows:

$$\rho = \rho_0 \mathrm{e}^{-\alpha y}, \quad P = P_0 \mathrm{e}^{-\alpha y}, \quad B_x = \sqrt{\frac{8\pi RT\rho}{\mu\beta}} \tag{41}$$

where $\alpha = g\rho_0/P_0\mu(1 + 1/\beta)$ is a parameter which is linearly dependent on gravity. These density, pressure, and magnetic field profiles given by Equation (41) were chosen as the initial

DOI: 10.1002/fld

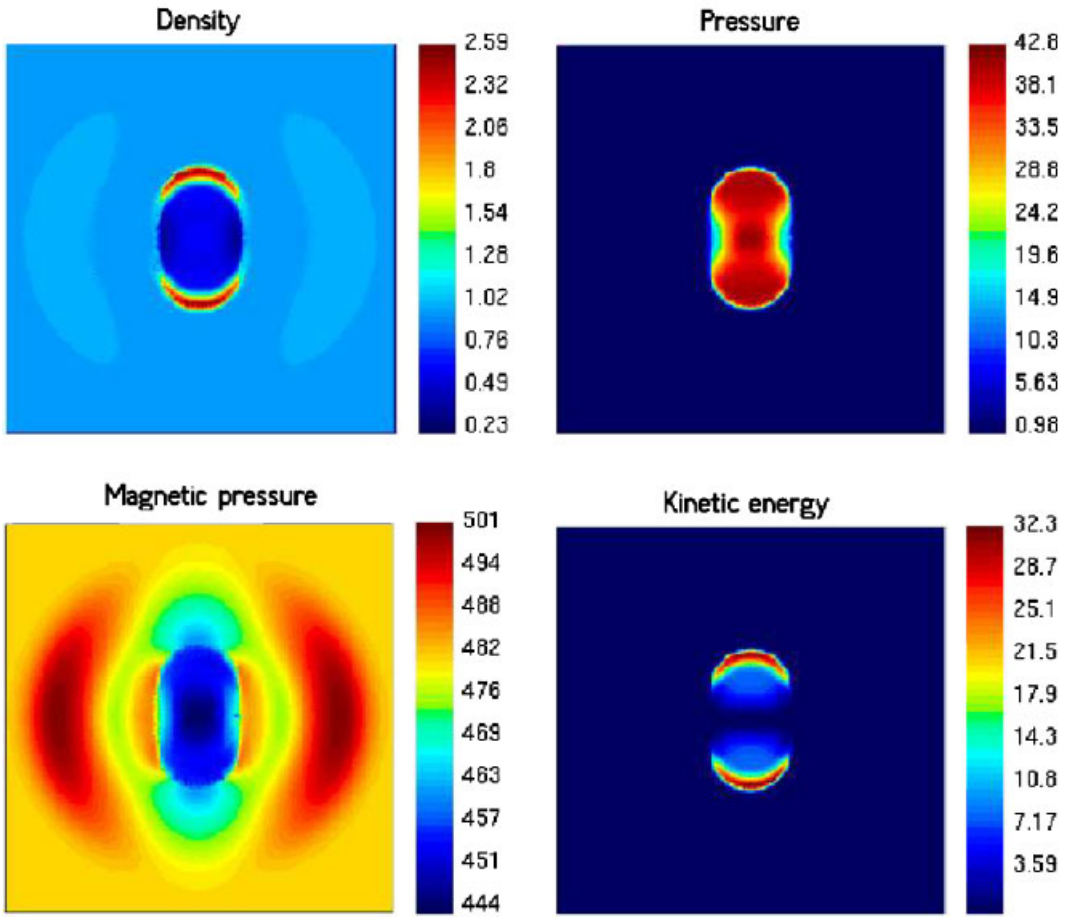

Figure 20. The solution of explosion case with $B_y = 100$ on 241×241 isotropic mesh at $t = 1$.

condition except in the explosion region. This problem was solved on isotropic triangular meshes of $x \in [0, 1]$, $y \in [0, 1]$ and all the boundaries were assumed to be outgoing (free) boundary. The explosion was initiated by releasing a higher pressure gas confined in a circular region into the medium. Since beta is assumed to be constant everywhere, the magnetic field also has a jump across the explosion boundary. Note that the solutions depend on four free parameters, namely, g, ρ_0, P_0 and β. In order to obtain solutions suitable for the comparison with the results given in Reference [27] (in which $\mu = 0.83$ was taken), the initial explosion radius was chosen to be $r = 0.022$ and the free parameters were adjusted as: $\rho_0 = 1$, $\beta = 1$, $P_0 = 0.15$, and $g = 1$. The time history of resulting density and Mach number colour graphs are presented in Figure 21. As seen, the explosion region expands and becomes anistropic due to the horizontal magnetic field and vertical gravity and a shock front appears along vertical direction since Mach number reaches $M = 1.16$. These results agree with those presented by Reference [27] in which astrophysical units were considered. In this reference, density and Mach number profiles (at $t = 0$, 5.2, and 10.6 Myr)

DOI: 10.1002/fld

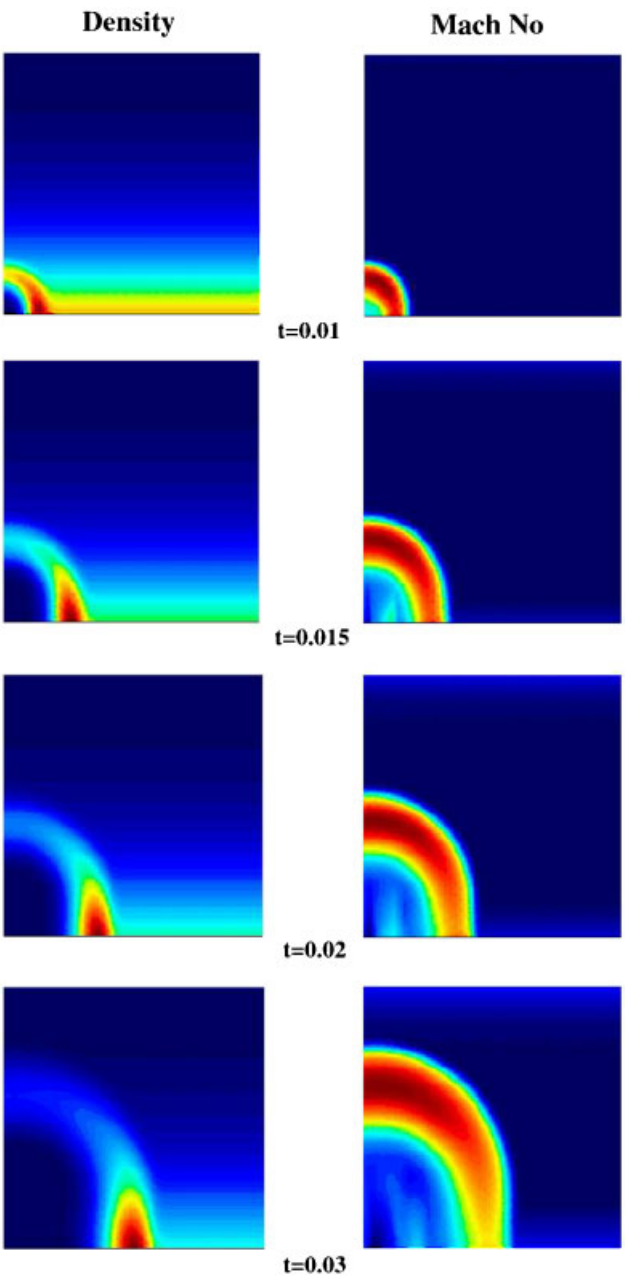

Figure 21. Density and Mach number graphs for obtained at different times for $\beta = 1$, $g = 1$ and $\rho_0 = 1$.

are given as a function of the vertical direction. Although the normalizations in this paper and those in Reference [27] are different, we can compare our results by following the location of the shock wave expanding towards mesh boundaries. Figure 5 of Reference [27] shows that the shock

DOI: 10.1002/fld

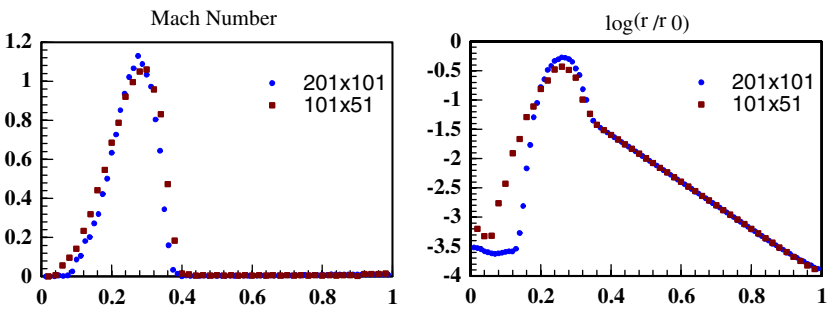

Figure 22. Mach number and density profiles in vertical direction at $x = 0$ obtained at $t = 0.015$ for two different meshes of 101×51 and 201×101.

front is located near $y = 0.33 y_{\max}$ (while $y_{\max} = 900\,\mathrm{pc}$) at $t = 5.2\,\mathrm{Myr}$ and $\log(\rho/\rho_0)$ reduces to -3.5 near centre and maximizes at -0.4 before the shock front. The y-profile of our solutions obtained by adjusting free parameters are given in Figure 22. This figure shows that (although solutions are diffused a little bit), the shock front is nearly at $y = 0.35 y_{\max}$ (while $y_{\max} = 1$) at $t = 0.015$ and $\log(\rho/\rho_0)$ reduces to -3.6 near centre and maximizes at -0.25. This is a reasonably good agreement with Reference [27] showing that the code presented here can be used for the astrophysical problems including magnetic fields and gravity.

7. CONCLUSION

The numerical solutions of MHD equations in two dimensions using the new wave model MHD-B in a fluctuation splitting scheme with the dual time stepping technique are presented. The space accuracy of model MHD-B is close to second-order and the accuracy of the time integration is high order by means of multistage time stepping algorithms. The pseudo time stepping was successfully employed between the time levels in order to reduce the $\nabla \cdot \mathbf{B}$ errors. The scheme contains the gravitational effects and it can easily be modified to include external fields and viscous effects. The test problems and accuracy graphs presented show that the code is robust and accurate and that it can be safely used for nonlinear compressible flows.

ACKNOWLEDGEMENTS

N. A. acknowledges the partial support from NATO Collaborative studies. The encouragements during the preparation of this manuscript and memory of T. Sarıgul for his daughter will never be forgotten by Ş. B.

REFERENCES

1. Colella P, Woodward P. The piecewise parabolic method (PPM) for gasdynamical simulations. *Journal of Computational Physics* 1984; **54**:174–201.
2. Roe PL. Discrete models for the numerical analysis of time-dependent multidimensional gas dynamics. *Journal of Computational Physics* 1986; **63**:458–476.
3. Harten A, Enquist BE, Osher SJ, Chakravarthy SR. Uniformly high order accurate essentially non-oscillatory schemes III. *Journal of Computational Physics* 1987; **71**:231–303.

DOI: 10.1002/fld

4. Roe PL. Fluctuations and signals a framework for numerical evaluation problems. *Numerical Methods for Fluid Dynamics*, Morton IKW, Baines IJ (eds). Academic Press: New York, 1982; 219–257.
5. Roe PL. Linear advection schemes on triangular meshes. Cranfield Institute of Technology CoA. *Report No. 8720*, Cranfield, Bedford, U.K., November 1987.
6. Aslan N. MHD-A: a fluctuation splitting wave model for planar magnetohydrodynamics. *Journal of Computational Physics* 1999; **153**:437–466.
7. Balcı Ş. The numerical solutions of two dimensional MHD equations by fluctuation splitting scheme on triangular meshes. *Ph.D. Thesis*, Physics Department, University of Marmara, Science-Art Faculty, İstanbul, Turkey, 2000.
8. Aslan N. Computational investigations of ideal MHD plasmas with discontinuities. *Ph.D. Thesis*, Nuclear Engineering Department, University of Michigan, U.S.A., 1993.
9. Powell KG. An approximate Riemann solver for magnetohydrodynamics (that works in more than one dimension). *ICASE Report No*: *94-24*, Langley, VA, 1994.
10. Aslan N, Kammash T. A new scheme for the numerical solutions of multidimensional MHD equations. *ICASE/LaRC Workshop on Barriers and Challenges in CFD*, Hampton, VA, U.S.A., August 1996; 5–7.
11. Aslan N, Kammash T. A Riemann solver for two dimensional MHD equations. *International Journal for Numerical Methods in Fluids* 1997; **25**:953–957.
12. Dai W, Woodward PR. On the divergence-free condition and conservation laws in numerical simulations for supersonic magnetohydrodynamic flows. *Astrophysics Journal* 1998; **494**:317–335.
13. Toth G. The div $B = 0$ constraint in shock-capturing magnetohydrodynamic codes. *Journal of Computational Physics* 2000; **161**:605–652.
14. Dedner A, Kemm F, Krner D, Munz CD, Schnitzer T, Wesenberg M. Hyperbolic divergence cleaning for the MHD equations. *Journal of Computational Physics* 2002; **175**:645–673.
15. Dailey LD, Pletcher RH. Evaluation of multigrid acceleration for preconditioned time accurate Navier–Stokes algorithms. *Computers and Fluids* 1996; **25**(8):791–811.
16. Shu CW. Total-variation-diminishing time discretizations. *SIAM Journal on Scientific and Statistical Computing* 1988; **9**:1073.
17. de Palma P. Investigations of Roe's 2D wave decomposition models for the Euler equations. *Technical Report*, Von Karman Institute for Fluid Dynamics, Lecture Series 1990-08, June, 1990.
18. Sweby PK. High resolution schemes using flux limiters for hyperbolic conservation laws. *SIAM Journal on Numerical Analysis* 1984; **21**:995–1011.
19. Sidilkover D, Roe PL. Unification of some advection schemes in two dimensions. *Technical Report 95-10*, ICASE, 1995.
20. Aslan N, Balcı Ş, Kammash T. Fluctuation splitting schemes on triangular grids for Euler and MHD equations with wave models. *Numerical Methods in Laminar and Turbulent Flow*, *Proceedings of the Tenth International Conference*, vol. 10, Swansea, 21–25 July 1997.
21. Aslan N, Kammash T, Balcı Ş. MHD-A: a new wave model for magnetohydrodynamics equations. *Godunov Symposium*, University of Michigan, Ann Arbor, 1–2 May 1997.
22. Balcı Ş, Aslan N. The numerical solutions of two dimensional Euler and MHD equations by fluctuation splitting scheme on triangular meshes. TFD 17. *Physics Symposium*, Alanya, Turkey, 27–31 October 1998.
23. van der Weide E. Compressible flow simulation on unstructured grids using multidimensional upwind schemes. *Ph.D. Thesis*, Technical University of Delft, Germany, November 1998.
24. Frank A, Jones TW, Ryu D, Gaalaas J. The magnetohydrodynamic Kelvin–Helmholtz instability: a two dimensional numerical study. *The Astrophysical Journal* 1996; **460**:777–793.
25. Linde TJ. A three dimensional adaptive multifluid MHD model of the heliosphere. *Dissertation*, University of Michigan, 1998.
26. Tang H-Z, Xu K. A high order gas kinetic method for multidimensional ideal magnetohydrodynamic. *Journal of Computational Physics* 2000; **165**:69–88.
27. Mineshige S, Shibata K, Shapiro PR. Large scale explosions and superbubbles in the galactic disk and halo I. Magnetohydrodynamic simulations. *The Astrophysical Journal* 1993; **409**:663–681.

DOI: 10.1002/fld